ACS APPLIED MATERIALS & INTERFACES

Research Article

www.acsami.org

Solution-Deposited F:SnO_2/TiO_2 as a Base-Stable Protective Layer and Antireflective Coating for Microtextured Buried-Junction H_2-evolving Si Photocathodes

Matthew G. Kast, Lisa J. Enman, Nicholas J. Gurnon, Athavan Nadarajah, and Shannon W. Boettcher*

Department of Chemistry and Biochemistry, University of Oregon, Eugene, Oregon 97403, United States

Supporting Information

ABSTRACT: Protecting Si photocathodes from corrosion is important for developing tandem water-splitting devices operating in basic media. We show that textured commercial Si-pn$^+$ photovoltaics protected by solution-processed semiconducting/conducting oxides (plausibly suitable for scalable manufacturing) and coupled to thin layers of Ir yield high-performance H_2-evolving photocathodes in base. They also serve as excellent test structures to understand corrosion mechanisms and optimize interfacial electrical contacts between various functional layers. Solution-deposited TiO_2 protects Si-pn$^+$ junctions from corrosion for ~24 h in base, whereas junctions protected by F:SnO_2 fail after only 1 h of electrochemical cycling. Interface layers consisting of Ti metal and/or the highly doped F:SnO_2 between the Si and TiO_2 reduce Si-emitter/oxide/catalyst contact resistance and thus increase fill factor and efficiency. Controlling the oxide thickness led to record photocurrents near 35 mA cm^{-2} at 0 V vs RHE and photocathode efficiencies up to 10.9% in the best cells. Degradation, however, was not completely suppressed. We demonstrate that performance degrades by two mechanisms, (1) deposition of impurities onto the thin catalyst layers, even from high-purity base, and (2) catastrophic failure via pinholes in the oxide layers after several days of operation. These results provide insight into the design of hydrogen-evolving photoelectrodes in basic conditions, and highlight challenges.

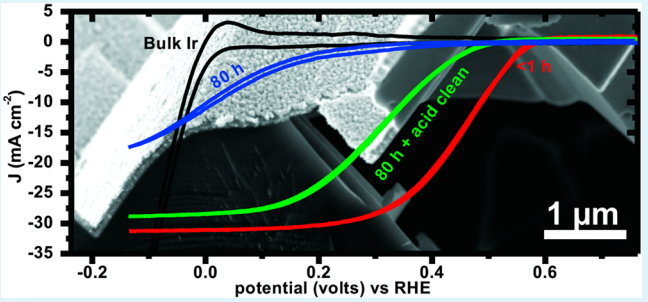

KEYWORDS: *solar, hydrogen, photocathode, protective layer, failure mechanism, alkaline electrolyte*

1. INTRODUCTION

Proposed tandem water-splitting devices utilize photocathodes and photoanodes in direct contact with the electrolyte. Tandems offer higher efficiency than single-junction devices because the individual junctions can each have smaller band-gaps and thus higher photocurrents in sunlight while still providing, in combination, the voltage needed to drive the thermodynamics and kinetics of water splitting (~1.6−1.8 V).[1] Chemically protecting semiconductor absorbers with good optoelectronic properties is important to enable high efficiency and long-term stability. Basic media is promising for scalable tandem photoelectrochemical water splitting because the oxygen evolution reaction (OER) catalysts with the highest activity, which are also earth abundant, are only stable under basic conditions (e.g., $Ni_xFe_{1-x}OOH$ and variants).[2−6] No known earth-abundant OER catalysts are stable in acid.[3] Use of neutral pH is challenging due to slow buffer-ion transport.[7] This suggests that the hydrogen evolution reaction also be carried out in base.

Si is a promising small-band gap material for a tandem device.[1,8] Unfortunately, Si and most other small (~1 eV) band gap absorbers are unstable and soluble in base, thus protective layers are needed.[9] Significant work has focused on the photoelectrochemical properties of unprotected and protected Si photoelectrodes in acid with Pt catalysts.[10−22] The protective layers have consisted of TiO_2,[23−25] F:SnO_2,[26] and thin SiO_2.[27] Recent work has also shown the use of MnO_x,[28] NiO_x,[29] CoO_x,[30] Ir,[31] and C- or N-doped TiO_2[32] as a protective coating on Si under OER conditions. Because of the range of oxidation states of Mn, Ni, and Co, it is unclear if these films would be stable to reduction at the cathodic hydrogen evolution reaction (HER) potentials, thus these oxides are perhaps less useful for the protection of photocathodes. Metallic protective coatings are not ideal because of parasitic light absorption. Oxide protective layers are usually deposited by sputtering[24,31] or atomic layer deposition (ALD)[16,17,23,28,32] and may be difficult and/or costly to scale. In summary, the ideal protective coating would be deposited inexpensively, optically transparent, thermodynamically stable, and composed of earth-abundant elements.

Here we use commercial Si solar cells as a test platform for studying solution-deposited protective coatings. By using a single commercial cell there is good consistency between the solid-state junction of all of the devices fabricated, which allows

Received: October 13, 2014
Accepted: December 3, 2014
Published: December 3, 2014

for a better understanding of the effect of the protective coating on the operation of the device. This also enabled the solid-state characteristics to be compared to the photoelectrochemical characteristics of different devices in acid and base. By controlling the thickness of the oxide protection layer we demonstrate good antireflection properties on the textured Si surface and thus high one-sun photocurrents near 35 mA cm^{-2} in some devices. We show that solution-deposited TiO_2 on solution-deposited F:SnO_2 makes ohmic contact to Si while preventing its corrosion in base for 24 h. Oxidized Ir, being the highest activity HER catalyst in base (see below), is used to demonstrate cells with photocathode efficiencies of up to 10.9%, which appears to be a new record.[33]

2. EXPERIMENTAL SECTION

2.1. Electrode Fabrication. Modified solar cells lacking top contacts, and in some cases lacking antireflective (AR) coatings, with phosphorus-rich glass or thermally grown SiO_2 in place of the AR coating, were a gift from Solar World. The solar cells had a p-type base (absorber) with a thin n^+ phosphorus-doped emitter (~100 nm in thickness) and had pyramidal surface texture 0.5−2 μm in depth. SiN_x AR coatings, if present, were removed by a 3 h etch in 48% HF. Phosphorus-rich glass was removed with 10−15 min etch in 48% HF. SiO_2 was removed with a 2−10 min etch in 20:1 BOE. Control electrodes on n^+ or p^+-Si were fabricated by making ohmic contact to the back of the Si with InGa eutectic and silver paint. Buried junction electrodes were fabricated by using silver paint to connect Sn−Cu wire to the Al back contact of the cell. Epoxy and glass tubing were used to isolate all but the Pt or Ir surface from the solution. All electrodes were ~0.5 cm by 0.5 cm.

2.2. Protective Layer Fabrication. F:SnO_2 was deposited via spray pyrolysis of 0.45 M dibutyl tin dichloride and 0.05 M ammonium fluoride in 95% ethanol 5% water.[34] A sample was placed on a hot plate with a surface temperature of 400 °C and allowed 1 min to come to temperature. A ring stand was used to hold an airbrush (Aztec A220 Broad Stroke) at a constant angle and distance from the sample. Two 1 s bursts were sprayed every 15 s, samples were rotated 1/4 of a turn every minute, with a second set of rotations starting $^1/_8$ of a turn off the first set. Deposition for 8 min yielded 50−70 nm of F:SnO_2 on a planar substrate as measured by ellipsometry. TiO_2 was deposited via spray pyrolysis of 0.05 M titanium n-butoxide and 0.1 M acetylacetonate in ethanol using the same procedure.[35] Deposition for 12 min yielded 50−70 nm of TiO_2 on a planar substrate as measured by ellipsometry.

2.3. Metallic Interface Layer and Catalyst Deposition. Ti, Ir, and Pt were evaporated via e-beam in an Angstrom Engineering Amod physical vapor deposition system. Catalyst control films of Pt and Ir were fabricated by depositing 50 nm of Pt or Ir onto 25 nm of Ti previously deposited onto a piranha (3:1 conc. aq. H_2SO_4: 30% aq. H_2O_2) and O_2 plasma (150 W for 5 min) treated glass microscope slides. Thin catalyst controls were made by depositing 2 nm of Ir onto clean Au/Ti coated glass slides. Silver paint was used to connect a Sn−Cu wire to the top surface and encased in epoxy. All photocathodes utilize 2 nm thick Ir/IrOx catalyst layers. A cross-section of the photoelectrodes is depicted in Figure 1, after deposition of the protective coatings and the catalyst layer.

2.4. Electrochemical Measurements. (Photo)electrochemical experiments were carried out with the fabricated working (photo)-electrode, a Pt counter electrode (in a separate compartment behind a high porosity plastic frit) and a Hg/HgO reference electrode. The electrolyte was 0.1 M UltraPure (Fluke Analytical TraceSelect,"UP") KOH, 1 M UP KOH or 1 M SemiGrade (Sigma-Aldrich Semiconductor grade 99.99%) KOH. High-purity H_2 gas was bubbled through the solution to maintain a constant dissolved H_2 concentration, and thus solution potential, during the measurements. $Ni(OH)_2$ deposition on Ir and Pt was from a 2 mM $NiCl_2$ solution with a carbon mesh counter electrode and a standard calomel reference electrode. Cleaning of the electrodes by cycling in acid was carried out in 1 M $HClO_4$ (Fluka TraceSelect).

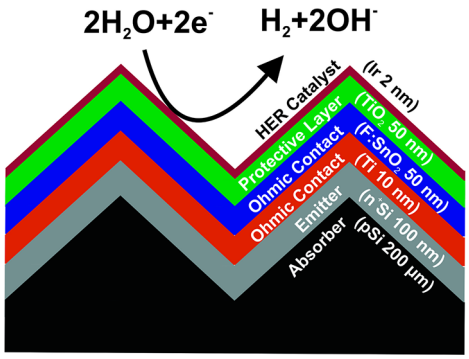

Figure 1. Schematic of protected textured cells with catalyst and interface layers. The role of each layer in electrode function and surface protection is discussed in the text and compared with control electrodes with different surface layers.

2.5. Reflectivity Measurements. Reflectivity measurements were performed on a PerkinElmer Lambda-1050 UV/vis/NIR spectrophotometer utilizing deuterium (short wavelengths) and tungsten-halogen (long wavelengths) light sources. An integrating sphere was used to collect the specular and diffuse reflectance at 1 nm intervals utilizing Si PMT (shorter wavelengths) and InGaAs (longer wavelengths) detectors. A 1.8 mm thick sheet of soft glass was mounted on the UV/vis/NIR instrument; samples were covered in water and quickly placed against the glass where they were held by surface tension and tape during the measurement, as is illustrated in Figure 8.

2.6. Physical Characterization. Scanning electron microscopy images were taken on a Zeiss Ultra-55 at 5 keV with an in-lens detector. X-ray photoelectron spectra were collected on a Thermo Scientific ESCALAB 250 using a monochromated Al Kα source. Ellipsometry measurements were taken on a Woollam M44 spectroscopic ellipsometer using 400 to 700 nm wavelength light. X-ray diffraction measurements were taken on a Rigaku SmartLab with parallel beam optics, in a θ−2θ geometry with a Cu Kα source.

3. RESULTS AND DISCUSSION

An ideal H_2-evolving photocathode could consist of a stable, high-efficiency buried junction electrically coupled to a high-activity catalyst. The protective coating should be thermodynamically stable in base, completely lack pinholes or other defects, have a low resistance to electron transport, be optically transparent, and have its thickness and index of refraction tuned for antireflection properties. Furthermore, for scalability, low-cost high-throughput methods are needed for deposition of the protective coating. The use of ALD for example, which is known to deposit at 100−300 nm h^{-1}, for thick film deposition could be difficult to scale.[16,32,36]

3.1. Semiconducting Absorber Characterization. A commercial n^+-emitter/p-base Si solar cell with a pyramidal textured surface was used to provide a consistent and efficient buried junction. Figure 2 shows the current density−potential (JV) characteristics of a full cell (15.5 cm × 15.5 cm), a 0.5 cm × 0.5 cm diced cell, and a photocathode consisting of a 0.5 cm × 0.5 cm diced cell with all contacts and AR coating etched off and a 2 nm layer of Pt in acid (0.5 M H_2SO_4) evolving H_2. The V_{oc} (580 mV) is reduced in the diced cell compared to the full cell (618 mV), which we attribute to increased recombination at the cleaved edges. The fill factor of the full cell is reduced due to the contact resistance of the measurement leads. The V_{oc} of the Pt-containing photocathode (574 mV vs the reversible hydrogen electrode, RHE) is identical to that of the diced solid-

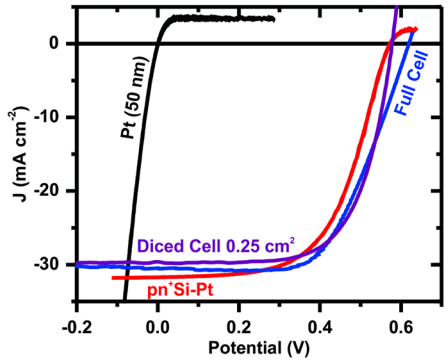

Figure 2. Comparison of *JV* curves from the full solid-state cell (15.5 cm × 15.5 cm), diced solid-state cell, and diced cell with Pt catalyst evolving hydrogen in the 0.5 M H_2SO_4 electrochemical cell (voltage referenced to RHE for electrochemical measurements). At Pt control electrode (black) is shown to indicate the origin of the loss in fill factor between the electrochemical (red) and solid state (purple) measurements.

state cell within sample-to-sample variability. The fill factor of the photocathode (58%) is reduced slightly compared to the diced solid-state cell (68%) due to the kinetic and mass-transport overpotentials of hydrogen evolution in acid on Pt. We note the photocathode efficiency of this cell for H_2-evolution is ~10.6%, higher than the previously reported 9.6% average for planar Pt-n$^+$p-Si.[10] This is only 1% less efficient than the solid-state diced cell (11.6%) because of a smaller fill factor caused by driving the electrochemical reaction. Improvements in edge passivation of the small devices used would be expected to significantly improve performance.

3.2. Solution-Deposition of Protective Coatings. Protective coatings were deposited from solution by spin-casting from an aqueous Sn(II) nitrate precursor[37] and by spray pyrolysis of tin butyl chloride and titanium isobutoxide precursors.[34,35] Spin-casting proved to be inappropriate due to the surface wetting properties of textured substrates resulting in deposition primarily in the valleys and not on the peaks of the textured surface (Figure 3A). Spray pyrolysis of F:SnO_2 and TiO_2 precursors yielded dense conformal coatings (Figure 3B) and was used for all other oxide depositions. This is likely because the precursor decomposes immediately to form dense crystalline oxide on the heated substrate surface during spray pyrolysis (see Figure S13 in the Supporting Information for diffraction data showing crystalline rutile F:SnO_2).

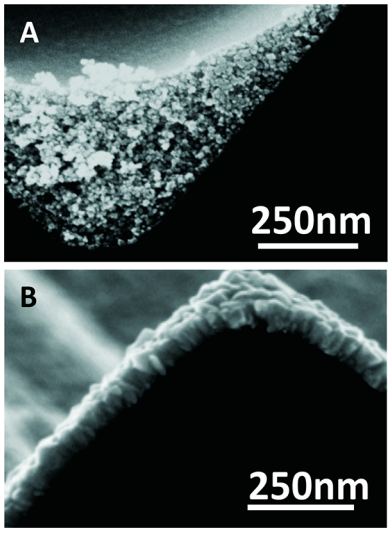

Figure 3. SEM images of F:SnO_2 deposited via (A) spin-casting and (B) spray pyrolysis.

3.3. Catalyst Selection and Thin Film Properties. To maximize the efficiency of a photoelectrode, we must minimize the overpotential of the reaction at the catalyst at the same time as the optical absorption of the catalyst is minimized.[38] We measured the activity of Pt films in acid (0.5 M TraceSelect H_2SO_4) and base (0.1 M ultrapure KOH) and compared it to the activity of Ir, IrO_x, and Ni(OH)$_2$-modified Pt and IrO_x films. We prepared IrO_x by cycling an Ir film at anodic potentials (0 to 0.7 V vs Hg/HgO) at 20 mV s^{-1} for 3 cycles. Subarraman et al. proposed that Ni(OH)$_2$ islands on Pt and Ir bulk metal electrodes increase the HER activity in base by affecting the rate-determining step of water adsorption to the catalyst surface.[39,38] We found that Ir with Ni(OH)$_2$ islands or IrO_x had the best activity for HER in base. This agrees with the work of Subarraman et al. on bulk metal electrodes with the caveat that the Ir likely oxidized during the anodic Ni(OH)$_2$ deposition. The high activity of Ni(OH)$_2$-Ir is thus perhaps due to IrO_x and not due to the effect of the Ni(OH)$_2$ islands as previously assumed; additional work is needed to clarify the mechanism.[40] Although IrO_x is not thermodynamically stable to reduction under HER conditions in base, others have shown IrO_x to have significant kinetic stability.[41] Electrodes were also tested in a solution of 0.1 M KOH containing 0.01 M LiOH. Although 0.01 M LiOH had a significant effect on the activity of Pt (and its Ni(OH)$_2$-modified analogue), its effect on the activity of IrO_x was small (Figure 4).

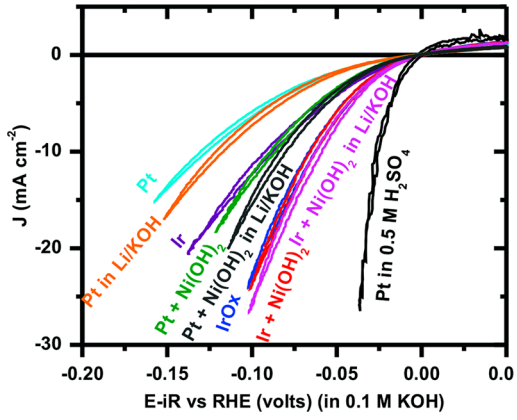

Figure 4. Voltammograms of HER catalysts in 0.1 M KOH contrasted to Pt in 0.5 M H_2SO_4. Some electrolytes also included 0.01 M LiOH, as indicated by the labels in the figure. Electrodes consist of 50 nm of Pt or Ir on 25 nm of Ti on glass. Ni(OH)$_2$ islands range from 1 to 25 monolayer equivalents in thickness. Scans were taken at 20 mV s^{-1}. The overpotentials of the different catalysts at 15 mA cm^{-2} are tabulated in Figure S11 in the Supporting Information.

3.4. Interfacial Si-Oxide-Catalyst Charge Transport. To achieve high efficiencies in the full H_2-evolving photocathode, low-resistance charge transport is needed from the n$^+$-Si emitter in the photovoltaic junction to the catalyst through the protective layer.[17] Because of the reactivity of Si, we found that the surface oxidizes during either spin-casting (and annealing) or spray pyrolysis. The interfacial SiO_2 led to higher series

resistance, which lowered the fill factor for photocathodes operating in base (e.g., see red curve Si−TiO_2−Ir in Figure 5).

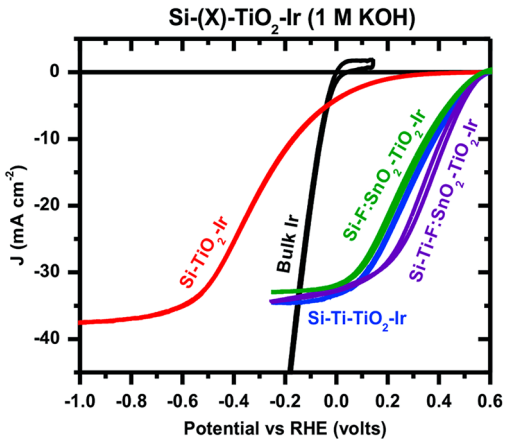

Figure 5. Voltammograms of different protective layer stacks showing the need for a Ti interface layer between TiO_2 and Si to maintain reasonably high fill factor.

The series resistance can be lowered by using F:SnO_2 to make the initial contact to the n^+-Si (e.g., see green curve Si−F:SnO_2−TiO_2−Ir in Figure 5), which is then further coated with TiO_2, needed for stability (see below). This is likely due to the higher carrier concentration in F:SnO_2, which increases tunnelling currents across the SiO_2 interfacial layer and allows the current to spread laterally and flow through locally thin SiO_2 regions. To further lower series resistance we deposited a thin layer of Ti (~10 nm thick) onto H-terminated Si prior to oxide deposition, as has been previously done by Seger et al.[15−17,24] The Ti is partially oxidized in air and further oxidized during spray pyrolysis or spin-casting. This results in a Si(pn^+)−Ti−TiO_2 interface between the n^+-Si emitter and the protective layer(s) (see below). Because of the work function alignment of Ti and n^+-Si, and small band offset between the conduction band of TiO_2 and the conduction band of Si, this interface has a low resistance for electron transport to the protective layer.[16,24] Further solution-deposition of F:SnO_2 and TiO_2 protection layers maintains a reasonably good fill factor and provides good chemical protection, as discussed below.

To further understand the interface reactivity, depth-profile XPS measurements were performed on F:SnO_2-coated planar Si control samples with 5 and 10 nm of Ti at the interface. Samples with only 5 nm (Figure 6A) of Ti show the formation of interfacial SiO_2 while samples with 10 nm (Figure 6B) of Ti show no interfacial SiO_2. XPS measurements also show metallic Ti^0 at the Ti−Si interface in the case of the 10 nm Ti film (see Figure S9 in the Supporting Information). Direct electrical measurements were taken on planar n^+-Si samples with F:SnO_2 deposited on top of no Ti, 5 nm of Ti and 10 nm of Ti, using an Al top contact. Significant contact resistance is seen when no or only 5 nm of Ti is present (Figure 7). Upon comparing the photocathodes with identical solid-state junctions and identical catalyst layers it is also apparent that the Si(pn^+)−TiO_2−Ir sample (no Ti interlayer) had significant resistive losses (Figure 5).

3.5. Optical Antireflection Properties of Protective Layer Coatings. To maximize the J_{sc} and thus efficiency of a photocathode the optical losses must be minimized. This

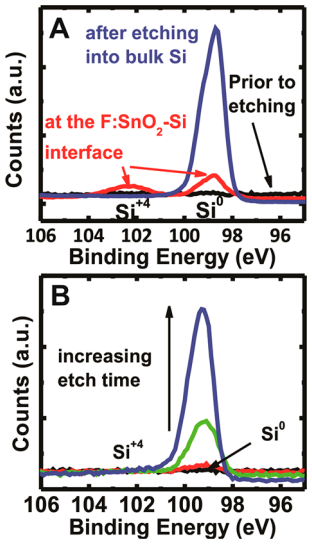

Figure 6. Depth profiled XPS of F:SnO_2−Ti−Si stacks. (A) Oxidized Si underneath a 5 nm thick layer of Ti. (B) No oxidized Si under 10 nm of Ti. XPS data showing the presence of metallic Ti at the Si surface is shown in Figure S9 in the Supporting Information.

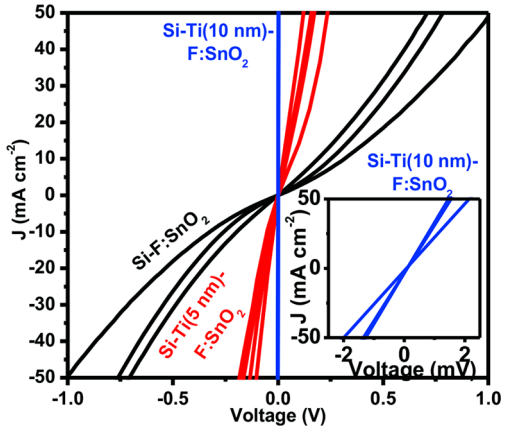

Figure 7. Comparison of solid-state *JV* behavior of n^+Si−F:SnO_2−Al stacks with and without 5 and 10 nm of Ti in between the F:SnO_2 and Si. Curves of the same color represent different devices with nominally identical layer thicknesses.

includes not only the reflectivity and optical absorption of the catalyst as mentioned before but also the reflectivity of the device as a whole. To minimize the total device reflectivity a commercial textured (100) Si cell was used, resulting in increased light trapping due to an increased number of photon-substrate interactions. Furthermore, the effect of the TiO_2 protective layer thickness on the reflectivity of the device in water was probed (Figure 8) as well as the effect of the presence of the different layers (Ti, F:SnO_2, TiO_2, and Ir). We note that the index of refraction of water is different than air (1.33 vs 1) and that the absorption of water slightly alters the AM1.5 spectrum.[42]

All thicknesses of TiO_2 studied reduced the reflectivity of the sample across the majority of wavelengths. We find that for a textured Si-TiO_2 test architecture, 40 nm of TiO_2 provides near optimal antireflection properties when measured under a glass plate in water to mimic the cell architecture (Figure 8.), consistent with simulations (see Figure S1 in the Supporting Information). We note that the measured reflectivity of the AR-

dx.doi.org/10.1021/am506999p | ACS Appl. Mater. Interfaces 2014, 6, 22830−22837

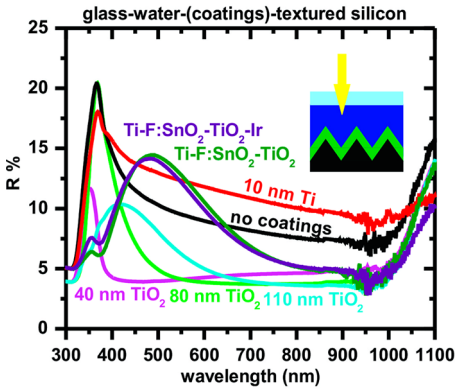

Figure 8. Reflectivity (percent) of textured silicon with 40, 80, and 110 nm of spray-deposited TiO_2 under water behind a glass slide. The minimum reflectivity is limited by the glass-air interface of the measurement cell (inset). Also, reflectivity of textured cells with Ti, $F:SnO_2-TiO_2$, $Ti-F:SnO_2-TiO_2$, and $Ti-F:SnO_2-TiO_2-Ir$ also taken under water behind glass as depicted. Ti layers are 10 nm thick, $F:SnO_2$ layers are 70 nm thick, TiO_2 layers are 50 nm thick (in multilayer stacks), and Ir layer is 2 nm thick. The minimum reflectivity is set by the outermost glass–air interface of ~4%.

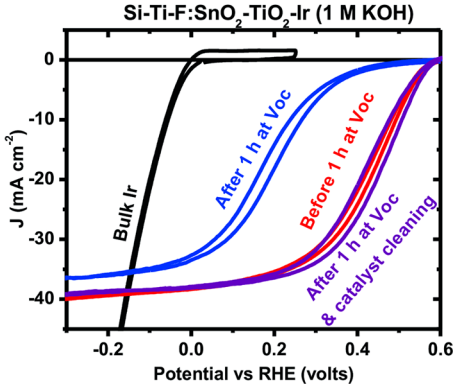

Figure 9. Voltamograms of $Ti-F:SnO_2-TiO_2$ protected silicon photocathodes under AM1.5 illumination.

coated textured samples in the visible region from 400 to 1000 nm (4.4–5.2%) is near that of the glass-air interface of the cell (~4%). The protective $Ti/F:SnO_2/TiO_2$ multilayers are more complicated to model as variation of the Ti, $F:SnO_2$, TiO_2, and Ir layers all effect the reflectivity of the sample because of the slight differences in the index of refraction in the $F:SnO_2$ and TiO_2 and the reflectivity and absorption of remaining metallic Ti. Experimental data for the protective stacks are shown in Figure 8. The addition of the 2 nm Ir layer has little effect on the reflectivity of the samples, while the Ti interface layer in the $Ti-F:SnO_2-TiO_2$ samples increases the reflectivity. Some of the Ti oxidizes in air upon placement on the hot plate during spray deposition of the oxide layers. The fabricated photoelectrodes with the $Ti/F:SnO_2/TiO_2$ protective coatings typically had larger total thickness (~110 nm) in order to improve durability. The 110 nm thick TiO_2 control films, however, only show an average reflectivity of only ~1% larger than the 40 nm thick films.

3.6. Champion Device Design. The champion device architecture achieved high photocurrents by utilizing a combined thickness of TiO_2 and $F:SnO_2$ (~100 nm), which provided reasonable antireflection properties, and the minimum amount of Ti needed to prevent oxidation at the Si/metal-oxide interface. To minimize interfacial resistance, we sequentially deposited 10 nm of Ti, 40 nm of $F:SnO_2$, and 60 nm TiO_2. IrO_x, which had the highest HER activity among the thin-films tested, was used as a catalyst to minimize losses due to kinetic overpotentials. The minimization of interfacial resistance and kinetic overpotential provides for good fill factors in the final device. The champion photocathode, operating in base, had an efficiency of 10.9% (Figure 9). Other devices of similar design made in a separate batch had efficiencies of 8.9 ± 0.7% (see Figure S2 in the Supporting Information). We note the relatively high variation between samples that are nominally identical. This is due to variation in J_{SC} and fill factor. J_{SC} depends on the reflectivity and absorption and thus on the thickness of the Ti, $F:SnO_2$, TiO_2, and Ir/IrO_x layers as well as the degree of oxidation of the Ti layer. The fill factor is particularly sensitive to oxidation of the Si to form a resistive SiO_2 interlayer (see Figure 7).

3.7. Failure Mode Analysis. For a photocathode to maintain high efficiency for long periods of time, the catalyst and absorber must both stay operational and in electrical contact. Possible failure modes include: dissolution of the catalyst, contamination/poisoning of the catalyst, dissolution of the protective layer (loss of contact between absorber and catalyst and eventual dissolution of buried junction), dissolution of the buried junction through pin holes in the protective layer, and oxidation of the buried junction resulting in high resistive losses. Here we analyze the various failure modes observed for the photoelectrode architecture developed.

After holding the champion protected Si device, $Si(pn^+)-Ti-F:SnO_2-TiO_2-Ir$, at open circuit for 1 h in base the fill factor was reduced significantly. Upon cleaning the catalyst by cycling to oxidizing potentials in 1 M $HClO_4$ the voltammogram was nearly identical to the first voltammogram (Figure 9). Thus, it is likely that the catalyst was poisoned by the reduction of transition metal impurities from the electrolyte while sitting at the cathodic V_{oc} (i.e., under H_2 with the surface at the equilibrium HER potential) and the reduced fill factor is due to an increased catalytic overpotential that is alleviated upon cleaning.[43] After prolonged polarization, Fe, Cu, and Pb were found via XPS analysis on the surface, whereas only Ir was found on the substrates initially (see Figure S12 in the Supporting Information).

Further stability testing of the champion device architecture was performed by holding near the maximum power point under illumination. After the initial 48 h, the V_{oc} decreased slightly and the fill factor decreased significantly. Upon cycling in acid (to remove metal surface contaminants), the fill factor returned to near that of the initial sweep, whereas the V_{oc} remained slightly less than that of the initial sweep, showing that either catalyst dissolution or damage to the buried junction had occurred (Figure 10). A plot of the current density as a function of time during the duration testing is shown in Figure S10 in the Supporting Information. After 80 h, substantial degradation had occurred. Visual inspection (after 80 h) showed small regions of discoloration (200–2000 μm^2) in the protective layer. In a representative region discoloured regions represented 5% of the area. Optical microscope images showed that the discolored regions were rectangular in shape, consistent with the known shape of etch pits on (100)-oriented Si. Cross-sectional SEM imaging confirmed that on the new device there was good adhesion between the protective/catalyst layer stack and the buried junction while the device run for 80 h in 1 M KOH showed multiple etch pits into the Si (Figure 11).

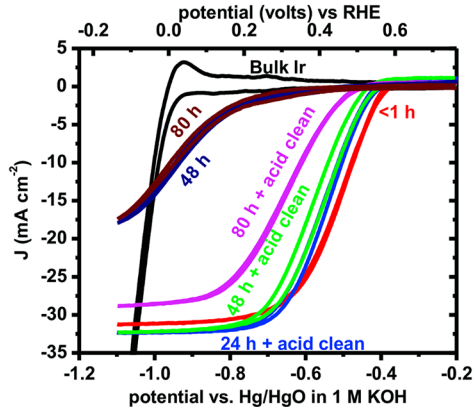

Figure 10. Voltammograms of photocathode after various times and treatments of stability testing. Stability testing was carried out at constant potential (300 mV positive of RHE) for various times. The photocathode was then cleaned in acid (1 M $HClO_4$) via cycling from reducing to oxidizing potentials.

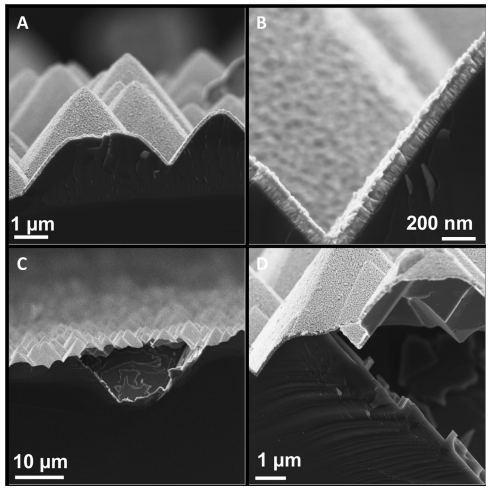

Figure 11. SEM images of protective layers (A, B) before duration testing, and (C, D) after 80 h of stability testing.

The buried junction is 100−200 nm deep, thus even relatively shallow etch pits can cause cross-junction shunting reducing the V_{oc}. The TiO_2 is apparently stable in 1 M KOH as the protective layer can be seen still intact and maintaining the pyramidal textured surface after duration testing (Figure 11). At shorter testing times (1−24 h), the device efficiency still drops considerably but is easily recovered upon cycling the device in 1 M $HClO_4$. To verify that a reduction in catalytic activity was the mode of short-term failure, we carried out identical stability testing on a 2 nm layer of Ir on Au (see Figure S6 in the Supporting Information). The catalytic activity decreased significantly after 24 h but can be recovered with cycling in acid. Such degradation of the HER activity of IrO_x has been observed previously.[41] These data provide evidence that short-term degradation is due to contamination of the catalyst by electroplating of solution impurities blocking the active Ir sites and long-term irreversible degradation is due to failure of the protective layer through pin-holes.

To better understand the long-term degradation mechanisms, we also tested Si(pn^+)−Ti−Ir and Si(pn^+)−Ti−F:SnO_2−Ir control devices. After holding a Si(pn^+)−Ti−Ir photocathode at open circuit for 1 h (see Figure S4 in the Supporting Information) the V_{oc} was significantly reduced and catalyst cleaning via anodic polarization did not restore the V_{oc} of the photocathode. The drop in V_{oc} suggests partial etching of the emitter caused shunt formation between the emitter and base layers of the buried junction (decreasing the V_{oc} by 59 mV for every order of magnitude increase in the dark current). Although dense TiO_2 should block base from reaching the Si, oxidation of Ti in base likely forms a porous hydrated oxide that allows electrolyte transport. After repeated cycling the fill factor of a Si(pn^+)−Ti−F:SnO_2−Ir protected photoelectrode also degraded with time (see Figure S5 in the Supporting Information). Anodic cleaning of the electrode did not recover the prior efficiency, thus eliminating catalyst contamination as the degradation mechanism. The V_{oc} and J_{sc} did not decrease, indicating that the solid-state buried junction remained intact. Because F:SnO_2 is known to have partial solubility in base,[44] dissolution of the F:SnO_2 resulting in loss of Ir is the likely cause of the performance degradation. These data thus illustrate the importance of the outermost dense TiO_2 layer for stability in the final devices.

4. CONCLUSION

Textured commercial solar cells can be used in conjunction with a thin layer of noble metal catalyst to test the stability and current−voltage characteristics of Si photocathodes operating in base at high photocurrents. Solution-processed stacks of F:SnO_2 and TiO_2 provide protection of the Si photocathode in base for ∼24 h and through interface control provide low resistance to charge transport. Reflection losses to a protective-layer-coated textured cell can be minimized with thicknesses near 40 nm, though thicker layers may be essential for protection. Integration of IrO_x catalyst led to photocathodes with >10% efficiency operating in base.

We also investigate the degradation mechanisms. Solution phase impurities in basic media remain a practical challenge when using thin catalyst films with low surface areas that can be easily covered with electrodeposited impurities. Rigorous precleaning of the electrolyte might (partially) alleviate these issues but were not investigated here. Such issues are not as severe in acid conditions because of the solubility of transition metals as well as the availability of higher-purity acid electrolytes.

Because of the presence of pinholes or other TiO_2 film defects, Si is slowly etched from under the protective layer forming large etch pits over the course of several days. Grain boundaries between the nanocrystalline TiO_2 may also play a role device failure. Protective schemes used in acid to protect Si do not have to contend with this issue as pinholes are passivated by the formation of insoluble SiO_2 in acid. ALD methods, which are non-line-of-sight and proceed through self-limiting surface reactions appear inherently better for the protection of nonplanar Si. Although it is unclear if classic ALD is scalable, other related methods such as liquid-phase ALD might allow for pinhole-free large-scale films to be deposited.[45] Solution-processing of thicker, more-conductive stable materials (Nb-doped TiO_2 is one possibility) might be able to provide long-term stability. In sum, these results illustrate the optical/electrical design principles behind efficient photocathode fabrication as well as remaining challenges.

■ ASSOCIATED CONTENT

Supporting Information

Figures S1−S13. This material is available free of charge via the Internet at http://pubs.acs.org/.

■ AUTHOR INFORMATION

Corresponding Author

*E-mail: swb@uoregon.edu.

Notes

The authors declare no competing financial interest.

■ ACKNOWLEDGMENTS

M.K. thanks Paul N. Plassmeyer and Adam M. Smith for assistance taking SEM images. This work was funded by National Science Foundation (NSF) grant CHE-1102637 through the Center for Sustainable Materials Chemistry. The CAMCOR shared instrument facilities are supported by grants from the W.M Keck Foundation, the M.J. Murdock Charitable Trust, ONAMI, the Air Force Research Laboratory (FA8650-05-1-5041), NSF (0923577 and 0421086), and the University of Oregon. S.W.B. acknowledges support from the Research Corporation for Science Advancement as a Cottrell Scholar.

■ REFERENCES

(1) Hu, S.; Xiang, C.; Haussener, S.; Berger, A. D.; Lewis, N. S. An Analysis of the Optimal Band Gaps of Light Absorbers in Integrated Tandem Photoelectrochemical Water-Splitting Systems. *Energy Environ. Sci.* **2013**, *6*, 2984.

(2) Danilovic, N.; Subbaraman, R.; Chang, K.; Chang, S. H.; Kang, Y. J.; Snyder, J.; Paulikas, A. P.; Strmcnik, D.; Kim, Y.; Myers, D.; Stamenkovic, V. R.; Markovic, N. M. Activity − Stability Trends for the Oxygen Evolution Reaction on Monometallic Oxides in Acidic Environments. *J. Phys. Chem. Lett.* **2014**, *5*, 2474−2478.

(3) McCrory, C. C. L.; Jung, S.; Peters, J. C.; Jaramillo, T. F. Benchmarking Heterogeneous Electrocatalysts for the Oxygen Evolution Reaction. *J. Am. Chem. Soc.* **2013**, *135*, 16977−16987.

(4) Trotochaud, L.; Ranney, J. K.; Williams, K. N.; Boettcher, S. W. Solution-Cast Metal Oxide Thin Film Electrocatalysts for Oxygen Evolution. *J. Am. Chem. Soc.* **2012**, *134*, 17253−17261.

(5) Pletcher, D.; Li, X. Prospects for Alkaline Zero Gap Water Electrolysers for Hydrogen Production. *Int. J. Hydrogen Energy* **2011**, *36*, 15089−15104.

(6) Trotochaud, L.; Young, S. L.; Ranney, J. K.; Boettcher, S. W. Nickel-Iron Oxyhydroxide Oxygen-Evolution Electrocatalysts: The Role of Intentional and Incidental Iron Incorporation. *J. Am. Chem. Soc.* **2014**, *136*, 6744−6753.

(7) Jin, J.; Walczak, K.; Singh, M. R.; Karp, C.; Lewis, N. S.; Xiang, C. An Experimental and Modeling/Simulation-Based Evaluation of the Efficiency and Operational Performance Characteristics of an Integrated, Membrane-Free, Neutral pH Solar-Driven Water-Splitting System. *Energy Environ. Sci.* **2014**, *00*, 1−10.

(8) Sun, K.; Shen, S.; Liang, Y.; Burrows, P. E.; Mao, S. S.; Wang, D. Enabling Silicon for Solar-Fuel Production. *Chem. Rev.* **2014**, *114*, 8662−8719.

(9) Glembocki, O. J.; Stahlbush, R. E.; Tomkiewicz, M. Bias-Dependent Etching of Silicon in Aqueous KOH. *J. Electrochem. Soc.* **1985**, *132*, 145−151.

(10) Boettcher, S. W.; Warren, E. L.; Putnam, M. C.; Santori, E. A.; Turner-Evans, D.; Kelzenberg, M. D.; Walter, M. G.; McKone, J. R.; Brunschwig, B. S.; Atwater, H. A.; Lewis, N. S. Photoelectrochemical Hydrogen Evolution Using Si Microwire Arrays. *J. Am. Chem. Soc.* **2011**, *133*, 1216−1219.

(11) Kargar, A.; Sun, K.; Jing, Y.; Choi, C.; Jeong, H.; Zhou, Y.; Madsen, K.; Naughton, P.; Jin, S.; Jung, G. Y.; Wang, D. W. Tailoring n-ZnO/p-Si Branched Nanowire Heterostructures for Selective Photoelectrochemical Water Oxidation or Reduction. *Nano Lett.* **2013**, *13*, 3017−3022.

(12) Laursen, A. B.; Pedersen, T.; Malacrida, P.; Seger, B.; Hansen, O.; Vesborg, P. C. K.; Chorkendorff, I. MoS_2 - an Integrated Protective and Active Layer on n^+p-Si for Solar H_2 Evolution. *Phys. Chem. Chem. Phys.* **2013**, *15*, 20000−20004.

(13) McKone, J. R.; Warren, E. L.; Bierman, M. J.; Boettcher, S. W.; Brunschwig, B. S.; Lewis, N. S.; Gray, H. B. Evaluation of Pt, Ni, and Ni−Mo Electrocatalysts for Hydrogen Evolution on Crystalline Si Electrodes. *Energy Environ. Sci.* **2011**, *4*, 3573.

(14) Reece, S. Y.; Hamel, J. a; Sung, K.; Jarvi, T. D.; Esswein, A. J.; Pijpers, J. J. H.; Nocera, D. G. Wireless Solar Water Splitting Using Silicon-Based Semiconductors and Earth-Abundant Catalysts. *Science* **2011**, *334*, 645−648.

(15) Seger, B.; Laursen, A. B.; Vesborg, P. C. K.; Pedersen, T.; Hansen, O.; Dahl, S.; Chorkendorff, I. Hydrogen Production Using a Molybdenum Sulfide Catalyst on a Titanium-Protected n(+)p-Silicon Photocathode. *Angew. Chem., Int. Ed.* **2012**, *51*, 9128−9131.

(16) Seger, B.; Tilley, D. S.; Pedersen, T.; Vesborg, P. C. K.; Hansen, O.; Grätzel, M.; Chorkendorff, I. Silicon Protected with Atomic Layer Deposited TiO_2: Durability Studies of Photocathodic H_2 Evolution. *RSC Adv.* **2013**, *3*, 25902.

(17) Seger, B.; Tilley, S. D.; Pedersen, T.; Vesborg, P. C. K.; Hansen, O.; Grätzel, M.; Chorkendorff, I. Silicon Protected with Atomic Layer Deposited TiO_2: Conducting versus Tunnelling through TiO_2. *J. Mater. Chem. A* **2013**, *1*, 15089.

(18) Sun, K.; Madsen, K.; Andersen, P.; Bao, W.; Sun, Z.; Wang, D. Metal on Metal Oxide Nanowire Co-Catalyzed Si Photocathode for Solar Water Splitting. *Nanotechnology* **2012**, *23*, 194013.

(19) Warren, E. L.; McKone, J. R.; Atwater, H. a.; Gray, H. B.; Lewis, N. S. Hydrogen-Evolution Characteristics of Ni−Mo-Coated, Radial Junction, n^+p-Silicon Microwire Array Photocathodes. *Energy Environ. Sci.* **2012**, *5*, 9653.

(20) Noh, S. Y.; Sun, K.; Choi, C.; Niu, M.; Yang, M.; Xu, K.; Jin, S.; Wang, D. Branched TiO_2/Si Nanostructures for Enhanced Photoelectrochemical Water Splitting. *Nano Energy* **2013**, *2*, 351−360.

(21) Nakato, Y.; Egi, Y.; Hiramoto, M.; Tsubomura, H. Hydrogen Evolution and Iodine Reduction on an Illuminated n-p Junction Silicon Electrode and Its Application to Efficient Solar Photoelectrolysis of Hydrogen Iodide. *J. Phys. Chem.* **1984**, *88*, 4218−4222.

(22) Nakato, Y.; Iwakabe, Y.; Hiramoto, M.; Tsubomura, H. Tungsten- or Molybdenum-Coated p-n Junction Silicon Electrodes for Efficient and Stable Photoelectrochemical Solar Energy Conversion. *J. Electrochem. Soc.* **1986**, *133*, 900−904.

(23) Chen, Y. W.; Prange, J. D.; Dühnen, S.; Park, Y.; Gunji, M.; Chidsey, C. E. D.; McIntyre, P. C. Atomic Layer-Deposited Tunnel Oxide Stabilizes Silicon Photoanodes for Water Oxidation. *Nat. Mater.* **2011**, *10*, 539−544.

(24) Seger, B.; Pedersen, T.; Laursen, A. B.; Vesborg, P. C. K.; Hansen, O.; Chorkendorff, I. Using TiO_2 as a Conductive Protective Layer for Photocathodic H_2 Evolution. *J. Am. Chem. Soc.* **2013**, *135*, 1057−1064.

(25) Lin, Y.; Battaglia, C.; Boccard, M.; Hettick, M.; Yu, Z.; Ballif, C.; Ager, J. W.; Javey, A. Amorphous Si Thin Film Based Photocathodes with High Photovoltage for Efficient Hydrogen Production. *Nano Lett.* **2013**, *13*, 5615−5618.

(26) Cox, C. R.; Winkler, M. T.; Pijpers, J. J. H.; Buonassisi, T.; Nocera, D. G. Interfaces between Water Splitting Catalysts and Buried Silicon Junctions. *Energy Environ. Sci.* **2013**, *6*, 532.

(27) Esposito, D. V.; Levin, I.; Moffat, T. P.; Talin, A. A. H_2 Evolution at Si-Based Metal-Insulator-Semiconductor Photoelectrodes Enhanced by Inversion Channel Charge Collection and H Spillover. *Nat. Mater.* **2013**, *12*, 562−568.

(28) Strandwitz, N. C.; Comstock, D. J.; Grimm, R. L.; Nichols-Nielander, A. C.; Elam, J.; Lewis, N. S. Photoelectrochemical Behavior of n-Type Si(100) Electrodes Coated with Thin Films of Manganese Oxide Grown by Atomic Layer Deposition. *J. Phys. Chem. C* **2013**, *117*, 4931−4936.

(29) Kenney, M. J.; Gong, M.; Li, Y.; Wu, J. Z.; Feng, J.; Lanza, M.; Dai, H. High-Performance Silicon Photoanodes Passivated with Ultrathin Nickel Films for Water Oxidation. *Science* **2013**, *342*, 836−840.
(30) Yang, J.; Walczak, K.; Anzenberg, E.; Toma, F. M.; Yuan, G.; Beeman, J.; Schwartzberg, A.; Lin, Y.; Hettick, M.; Javey, A.; Ager, J. W.; Yano, J.; Frei, H.; Sharp, I. D. Efficient and Sustained Photoelectrochemical Water Oxidation by Cobalt Oxide/Silicon Photoanodes with Nanotextured Interfaces. *J. Am. Chem. Soc.* **2014**, *136*, 6191−6194.
(31) Mei, B.; Seger, B.; Pedersen, T.; Malizia, M.; Hansen, O.; Chorkendorff, I.; Vesborg, P. C. K. Protection of p+-n-Si Photoanodes by Sputter-Deposited Ir/IrO. *J. Phys. Chem. Lett.* **2014**, *5*, 1948−1952.
(32) Hu, S.; Shaner, M. R.; Beardslee, J. a.; Lichterman, M.; Brunschwig, B. S.; Lewis, N. S. Amorphous TiO_2 Coatings Stabilize Si, GaAs, and GaP Photoanodes for Efficient Water Oxidation. *Science* **2014**, *344*, 1005−1009.
(33) Strmcnik, D.; Uchimura, M.; Wang, C.; Subbaraman, R.; Danilovic, N.; Van der Vliet, D.; Paulikas, A. P.; Stamenkovic, V. R.; Markovic, N. M. Improving the Hydrogen Oxidation Reaction Rate by Promotion of Hydroxyl Adsorption. *Nat. Chem.* **2013**, *5*, 300−306.
(34) Adnane, M.; Cachet, H.; Folcher, G.; Hamzaoui, S. Beneficial Effects of Hydrogen Peroxide on Growth, Structural and Electrical Properties of Sprayed Fluorine-Doped SnO_2 Films. *Thin Solid Films* **2005**, *492*, 240−247.
(35) Oja, I.; Mere, a.; Krunks, M.; Solterbeck, C.-H.; Es-Souni, M. Properties of TiO_2 Films Prepared by the Spray Pyrolysis Method. *Solid State Phenom.* **2004**, *99*−*100*, 259−264.
(36) Leskelä, M.; Ritala, M. Atomic Layer Deposition Chemistry: Recent Developments and Future Challenges. *Angew. Chem., Int. Ed.* **2003**, *42*, 5548−5554.
(37) Nadarajah, A.; Carnes, M. E.; Kast, M. G.; Johnson, D. W.; Boettcher, S. W. Aqueous Solution Processing of F-Doped SnO_2 Transparent Conducting Oxide Films Using a Reactive Tin(II) Hydroxide Nitrate Nanoscale Cluster. *Chem. Mater.* **2013**, *25*, 4080−4087.
(38) Trotochaud, L.; Mills, T. J.; Boettcher, S. W. An Optocatalytic Model for Semiconductor−Catalyst Water-Splitting Photoelectrodes Based on In Situ Optical Measurements on Operational Catalysts. *J. Phys. Chem. Lett.* **2013**, *4*, 931−935.
(39) Subbaraman, R.; Tripkovic, D.; Strmcnik, D.; Chang, K.-C.; Uchimura, M.; Paulikas, A. P.; Stamenkovic, V.; Markovic, N. M. Enhancing Hydrogen Evolution Activity in Water Splitting by Tailoring Li^+-$Ni(OH)_2$-Pt Interfaces. *Science* **2011**, *334*, 1256−1260.
(40) Danilovic, N.; Subbaraman, R.; Strmcnik, D.; Chang, K.-C.; Paulikas, a P.; Stamenkovic, V. R.; Markovic, N. M. Enhancing the Alkaline Hydrogen Evolution Reaction Activity through the Bifunctionality of $Ni(OH)_2$/metal Catalysts. *Angew. Chem., Int. Ed. Engl.* **2012**, *51*, 12495−12498.
(41) Burke, L. D.; Naser, N. S.; Ahern, B. M. Use of Iridium Oxide Films as Hydrogen Gas Evolution Cathodes in Aqueous Media. *J. Solid State Electrochem.* **2007**, *11*, 655−666.
(42) Döscher, H.; Geisz, J. F.; Deutsch, T. G.; Turner, J. A. Sunlight Absorption in Water − Efficiency and Design Implications for Photoelectrochemical Devices. *Energy Environ. Sci.* **2014**, *7*, 2951.
(43) Subbaraman, R.; Danilovic, N.; Lopes, P. P.; Tripkovic, D.; Strmcnik, D.; Stamenkovic, V. R.; Markovic, N. M. Origin of Anomalous Activities for Electrocatalysts in Alkaline Electrolytes. *J. Phys. Chem. C* **2012**, *116*, 22231−22237.
(44) Schweitzer, G. K.; Lester, L. P. *The Aqueous Chemistry of the Elements*; Oxford University Press: New York, 2010.
(45) Foong, T. R. B.; Shen, Y.; Hu, X.; Sellinger, A. Template-Directed Liquid ALD Growth of TiO_2 Nanotube Arrays: Properties and Potential in Photovoltaic Devices. *Adv. Funct. Mater.* **2010**, *20*, 1390−1396.